applied optics

# Tracking sub-nanometer thermal structural changes with speckle interferometry

Babak Saif,[1] Perry Greenfield,[2,*] Marcel Bluth,[3] Lee Feinberg,[1] J. C. Wyant,[4] and Ritva Keski-Kuha[1]

[1]NASA/GSFC, 8800 Greenbelt Road, Greenbelt, Maryland 20771, USA
[2]Space Telescope Science Institute, 3700 San Martin Drive, Baltimore, Maryland 21218, USA
[3]Intuitive Machines, 3700 Bay Area Blvd. #100, Houston, Texas 77058, USA
[4]College of Optical Sciences, University of Arizona, Tucson, Arizona 85721, USA
*Corresponding author: perry@stsci.edu

Received 1 April 2020; revised 11 June 2020; accepted 16 June 2020; posted 16 June 2020 (Doc. ID 394213); published 10 July 2020

**Based on our results of the James Webb Space Telescope (JWST) center-of-curvature tests where we were able to measure dynamic amplitudes of Zernike terms to the order of a few picometers, we have applied the same approach to determine if it is possible to measure the accuracy of higher-order Zernike terms as a function of time rather than frequency, i.e., static measurements in place of measuring the amplitude of frequency components. We have applied this approach to data taken for the JWST backplane structure test article (BSTA) in 2006 and find that we can measure effects at the sub-nanometer level, as small as 50 pm for Zernike terms over 30. We conclude that these results show it will be possible to use these techniques to ensure that the optics and support structure for large space telescopes can meet the necessary stability requirements for detecting spectral signatures of life on Earth-like extra-solar planets.** 

https://doi.org/10.1364/AO.394213

## 1. INTRODUCTION

Our analysis of the James Webb Space Telescope (JWST) primary mirror segments during the center-of-curvature tests performed in ambient conditions at Goddard Space Flight Center indicated that it was possible to measure high-order Zernike terms to high precision ([1]). This unexpected accuracy led us to wonder what was achievable for the data taken during the JWST backplane structure test article (BSTA) measurements made at Marshall Space Flight Center in 2006 where the stability of a prototype of part of the JWST backplane was measured with respect to temperature in vacuum and cryogenic temperatures. The results of that test were reported in Ref. [2]. Figure 1 shows a photograph of the structure that was studied. In other words, could we use substantial averaging (both temporal and spatial) to improve the accuracy of the measurements?

Note that the test of the JWST backplane was done only with the backplane structure using speckle interferometry. No optical surfaces were involved in this test, unlike the center-of-curvature tests, where only optical surfaces were tested and the behavior of the backplane inferred from the optical measurements. Another major difference between these tests was that the center-of-curvature tests were studying the dynamics of the optics in the presence of commanded mechanical stimulation to understand the dynamics of the whole structure. The BSTA test was to study the stability of the structure with regard to drifts in response to temperature changes at cryogenic temperatures.

The objective of the original BSTA test was to ensure the stability requirements for the backplane structure were met. As such, the focus was entirely on seeing that the necessary level of stability was achieved, not on the possible accuracy of the measurement well beyond that requirement. This reanalysis sought to determine how good the accuracy was for a large structure, albeit with the focus on static accuracy versus accuracy of measuring the amplitude of a small, known dynamic stimulation as was done with the center-of-curvature tests.

## 2. RE-ANALYSIS

We reprocessed the BSTA data with an aim of analyzing with respect to something like Zernike equivalent components. The structure was observed with a high power laser and used speckle interferometry at a rate of five frames per second. The full details of the instrumentation and the test configuration can be found in Ref. [2]. The original processing processed only about one frame per second since that was sufficient to achieve the accuracy to test whether the requirement was being met. In this case, we wanted as much data as possible, and this time we needed to process all the available data. The original processing used a proprietary phase unwrapping routine available only

**Fig. 1.** Photograph of the BSTA structure.

on a computing platform that is no longer available to us. The reprocessing used an open source spatial phase unwrapper available in the Python package scikit-image ([3]). Given the spindly nature of the spatial structure, the unwrapping occasionally had difficulty in unwrapping the phase in a self-consistent manner.

A short explanation of how speckle interferometry is different from that used for optical surfaces is in order. The speckle image consists of areas with widely differing phases such that a single image contains no useful information. However, if nothing changes between two successive exposures, the phase difference between the two exposures should be zero. Likewise, small surface displacements will result in a phase difference when subtracting the first image from the second (this description is somewhat simplified since the phase image is derived from the actual raw image by some processing). Thus it is necessary to pick a reference image to use for the differencing. To observe changes over time, one may use the same reference image, but only up to a point. Various changes, such as extreme tilt changes, may make it difficult to perform spatial phase unwrapping, and as a result, it is necessary to change reference images periodically. We refer to these reference images as baseline images, as they define the spans of time that use the same reference. The net change over time is essentially the sum of the accumulated changes over each baseline period.

This necessitated special handling of the processed images, mainly to (1) determine which images to retain for analysis, and (2) tie different baseline data together. Relying on one common image introduces extra noise into the accumulated results. The first issue was addressed by looking at each spatially unwrapped images, and if the adjacent segments displayed too-large a phase difference (i.e., greater than $\pi/4$), the image was rejected from being included in the results. In effect, this is rejection based on seeing too-large phase jumps in a spatial sense. The second was solved by overlapping baseline sets by 200 exposures, and then computing the cumulative offset based on the average offset in the overlapping differences.

More specifically, we select an image to use as a baseline by checking how many of the subsequent images using it have spatial phase unwrapping problems, and doing that for several potential baseline exposures. The one with the fewest rejected images using it as a reference image is the one selected as the baseline reference image. We then select the next baseline reference image in the same way. Each baseline reference image is used for that interval, plus 200 exposures beyond the next baseline reference image, ensuring that we have an overlap of 200 exposures to match the average difference in between baselines to use as the cumulative difference for that baseline set (even with exposure rejection, there were at least 150 exposures that overlapped). At five frames per second, this amounts to 40 s of overlap for a rebaselining period of approximately 10 min. This is done all through the full set of data for a continuous measurement of how the Zernike terms change over the whole set of data. Since the resulting phase image has had piston, tip, and tilt removed from the image, the first three Zernike terms are identically zero (Z0–Z2).

Based on previous analysis of the BSTA data, we knew that it was stable enough to use the same baseline exposure for 10 to 15 min. This formed the basis of where we started looking for a new baseline, e.g., in the range of 10 min plus or minus 100 exposures, or equivalently, plus or minus 20 s. The resulting average baseline interval was 587 s, and very nearly 1/3 of the exposures during the processing were discarded for analysis due to poor phase unwrapping results. This is higher than the rejection rate close to a baseline, where less than 50 out of 200 were rejected, since more problems occur the longer the time between the exposure and the baseline image.

The computation of the phase difference is somewhat more complicated than typical for optical surfaces. The signal-to-noise ratio is generally lower for speckle data, and so it is necessary to do some spatial averaging. This cannot be done on the computed phase difference, as it would not properly handle areas of phase wraps. The phase is computed from the values for four different interferometer phase delays (see [2]). The fundamental computation is the arctangent of the numerator and denominator terms. The spatial smoothing to both of these terms as a simple box filter, i.e., the average of all pixels within a box, is a $9 \times 9$ box in this instance. There is an implicit level of further spatial averaging in computing the Zernike terms since each term is based on all the pixels in the masked image.

The mask used for the data is shown in Fig. 2. Needless to say, it does not look much like a filled circle. Thus it is necessary to derive a set of orthogonal basis functions for this structure using the Gram–Schmidt technique in order to fit independent basic functions. This was done by first determining the smallest possible enclosing circle for the data in the image plane (shown in Fig. 2). A convex hull analysis was performed on the mask, and then the smallest enclosing circle was generated from the vertices of the convex hull using Python code available from https://www.nayuki.io/page/smallest-enclosing-circle to compute the smallest enclosing circle. The coordinates of the image data were transformed into the coordinate system where the enclosing circle's center is at 0, 0 and its radius is one. After this transformation, the Gram–Schmidt ortho-normalization was performed on the original Zernike basis set to produce a set of "modified" Zernike basis functions. The ANSI/OSA convention was used for the initial Zernike basis set. Hereafter in this section, all references to Zernike terms refer to this derived basis set.

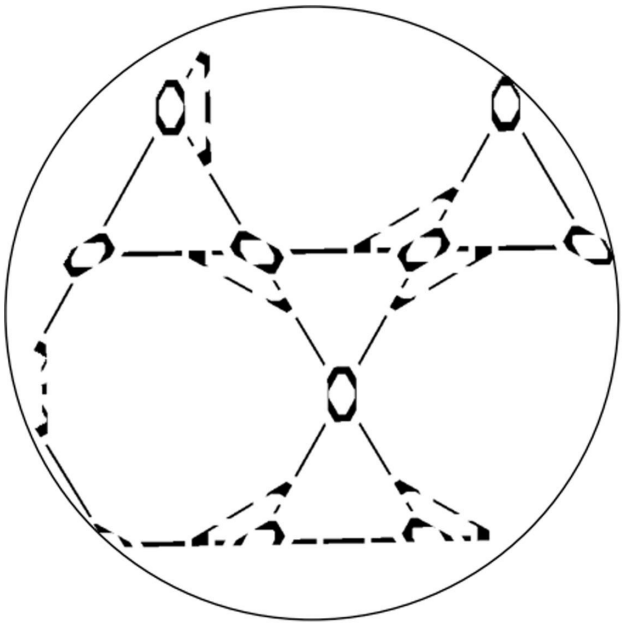

**Fig. 2.** Mask used for analysis of BSTA with the minimum enclosing circle over-plotted. Some areas of the structure are omitted due to insufficient illumination. The mask is narrower in general because of the 9 × 9 smoothing box used in the phase calculation to reduce the phase noise, thus reducing the area uncontaminated by the border by that many pixels. The enclosing circle is used to define the transform of the image pixel coordinates to that used for the original Zernike basis set, where the circle is at radius = 1, and the center is the origin of the coordinate system.

The data selected for analysis were taken during one of the temperature hold points (most of the data were obtained during cool down or warm up) where the structure was kept at a relatively constant temperature. The goal was to see how accurately we could measure the modified Zernicke terms for the structure. The data analyzed were taken on 12 September 2006 for approximately 4 h during a hold at approximately 60 deg Kelvin.

## 3. RESULTS

Figure 3 shows the Z3 term as a function of time with varying levels of binning sizes in time over-plotted, i.e., a bin size of 100 means 100 consecutive time sample values were averaged to produce one point in the plot. Figure 4 shows the same for Z35 with the same set of binning sizes. We estimate the accuracy of the binned data by computing the RMS of the differences between values (they are independent since no data points are shared in their averages). We then divide that RMS by $\sqrt{2}$ since the difference combines the errors of the two points in quadrature. For the Z3, we do this only for the first half of the data since that appears to have the least drift. The RMS value obtained for the 1000 binsize data is 0.9 nm. We do the same for the Z35 data over the whole time period since there is no lengthy drift-less segment. The RMS computed for those data is 14 pm.

In principle, we should be able to infer these RMS values from the RMS values of the unbinned data. That inference is shown in Fig. 5, which displays the result for the 36 Zernike

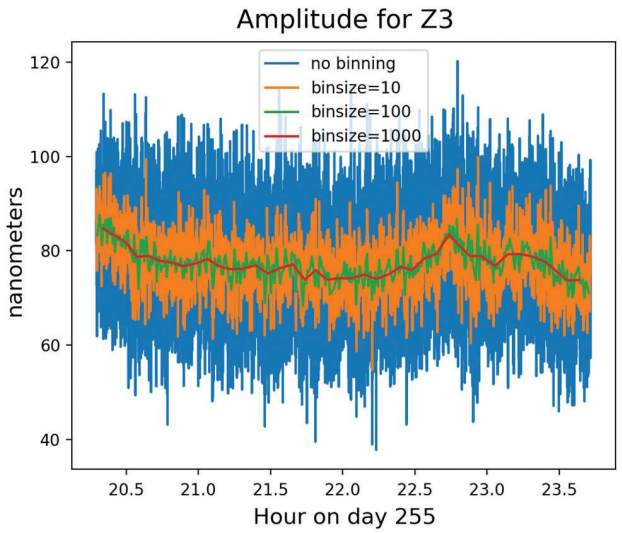


**Fig. 3.** Amplitude of the Z3 term as a function of time for various binning sizes where the data are binned in time. Blue is unbinned, orange a binning factor of 10, green a binning factor of 100, and red a binning factor of 1000.

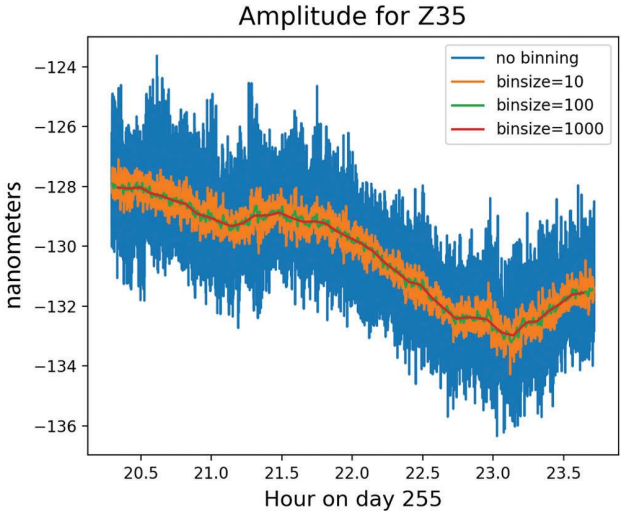


**Fig. 4.** Amplitude for the Z35 term as a function of time for various binning sizes where the data are binned in time. Colors are the same as for Fig. 3.

terms with two different scales shown. The scale on the left is the standard deviation computed for unbinned differences of adjacent measurements. From those values, we can infer the standard deviation for individual measurements assuming independence by dividing by $\sqrt{N}$. The scale on the right is what would be inferred from the original sampling if averaged over 1000 measurements. We see from that plot that the inferred RMS for Z3 is a factor of a few less than that measured directly from successive binned measurements, while the RMS for Z35 is roughly double that obtained from the successive binned measurements (recall that the plot values measured on the right scale must be divided by $\sqrt{2}$ to be compared to the RMS for individual measurements). There is rough agreement from the binned data from the inferred noise, suggesting that the noise is

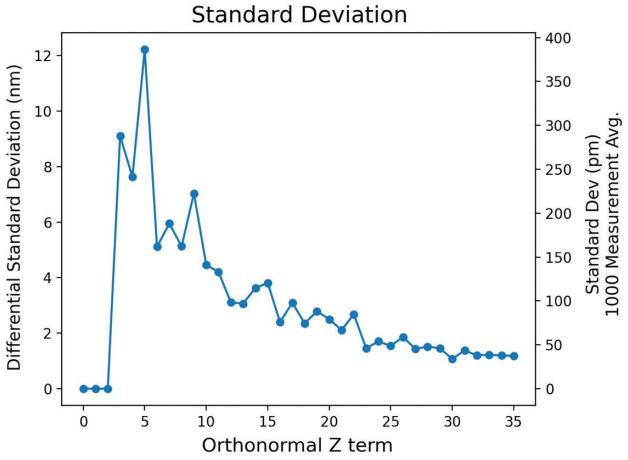


**Fig. 5.** This plot is to be interpreted in two different ways. The scale on the left side represents the computed differential RMS values between samples for each Z term. The inferred noise for a single sample is the value displayed divided by the square root of two. The scale on the right represents the expected RMS for 1000 averaged values. Since piston, tip, and tilt are removed from the final phase image, the first three Z terms are identically zero.

indeed independent in nature and that with sufficient averaging, quite accurate measurements can be made of individual Zernike terms, even for a complex structure.

## 4. CONCLUSION

These results demonstrate the level of accuracy possible when using a chamber that was not optimized for ultra-stability. This is relevant for future space telescopes because of their stringent stability requirements for observing Earth-like planets. For example, the requirements for the Large Ultra-Violet Optical Infra-Red telescope (LUVOIR) to obtain sufficiently good spectra from Earth-like planets to detect spectral signatures indicating the presence of life are on the orders of tens of picometers. This is documented in the LUVOIR final report submitted to the National Academy for consideration as part of the Astro2020 evaluation [4]. The key metric discussed in this report is exo-Earth yield, which is highly dependent on the diameter of the telescope due to its impact on both resolution and sensitivity. The report shows why smaller telescopes such as the alternative Habitable Exoplanet Observatory (HabEx) proposal [5] or smaller probe missions would therefore not match the yield of LUVOIR.

The critical stability driver is achieving a $10^{10}$ contrast ratio. A simulation of the required wavefront stability per aberration to achieve this can be found in the paper by Juanola-Parramon [6]. That paper shows the most sensitive aberrations are piston, tip, and tilt, and these require stability at about the level of 10 pm RMS, while other low-order aberrations can be on the orders of tens of picometers. This requirement assumes applying active control over an observation, and it includes all mechanical considerations such as dynamics and thermal control residuals for the mirrors and structure. The ultra-stable white paper [7] discusses the detailed challenges of the mirrors and structures that need to tally up to the 10 pm RMS residual surface errors after control for the tip, tilt, and piston requirements and the need for tens of picometers RMS residual after control for higher-order aberrations.

Even at the levels achieved, a thermal stability/distortion test is feasible at the LUVOIR level of requirements [4,7] using a 10 times extended variation to that expected to improve the accuracy of the measured effect, similar to the extended temperature variation applied on BSTA to measure its temperature sensitivity to better accuracy. However, with a more optimized environment, the level of extended variation could be even smaller, which indicates that this methodology can be used on future ultra-stable large telescopes. The applications include both assessing stability during the technology phase and in measuring primary mirror accuracy (possibly using partially ground mirrors as was done on JWST) and BSTA verification.

**Funding.** National Aeronautics and Space Administration; Space Telescope Science Institute.

**Disclosures.** The authors declare no conflicts of interest.

## REFERENCES

1. B. Saif, M. Bluth, P. Greenfield, W. Hack, B. Hoffmann Eegholm, P. Blake, R. Keski-Kuha, L. Feinberg, and J. W. Arenberg, "Measurement of large cryogenic structures using a spatially phase-shifted speckle pattern interferometer," Appl. Opt. **47**, 737–745 (2008).
2. B. Saif, D. Chaney, P. Greenfield, M. Bluth, K. Van Gorkom, K. Smith, J. Bluth, L. Feinberg, J. Wyant, M. North-Morris, and R. Keski-Kuha, "Measurement of picometer-scale mirror dynamics," Appl. Opt. **56**, 6457–6465 (2017).
3. S. van der Walt, J. L. Schönberger, J. Nunez-Iglesias, F. Boulogne, J. D. Warner, N. Yager, E. Gouillart, and T. Yu, and the scikit-image contributors, "Scikit-image: image processing in Python," PeerJ **2**, e453 (2014).
4. M. R. Bolcar, J. Crooke, J. E. Hyland, G. Bronke, C. Collins, J. Corsetti, J. Generie, Q. Gong, T. Groff, W. Hayden, A. Jones, B. Matonak, S. Park, L. Sacks, G. West, K. Yang, and N. Zimmerman, "Space telescopes and instrumentation 2018: optical, infrared, and millimeter wave," Proc. SPIE **10698**, 106980O (2018).
5. B. S. Gaudi, S. Seager, B. Mennesson, A. Kiessling, K. Warfield, K. Cahoy, J. T. Clarke, S. Domagal-Goldman, L. Feinberg, O. Guyon, J. Kasdin, D. Mawet, P. Plavchan, T. Robinson, L. Rogers, P. Scowen, R. Somerville, K. Stapelfeldt, C. Stark, D. Stern, M. Turnbull, R. Amini, G. Kuan, S. Martin, R. Morgan, D. Redding, H. P. Stahl, R. Webb, O. Alvarez-Salazar, W. L. Arnold, M. Arya, B. Balasubramanian, M. Baysinger, R. Bell, C. Below, J. Benson, L. Blais, J. Booth, R. Bourgeois, C. Bradford, A. Brewer, T. Brooks, E. Cady, M. Caldwell, R. Calvet, S. Carr, D. Chan, V. Cormarkovic, K. Coste, C. Cox, R. Danner, J. Davis, L. Dewell, L. Dorsett, D. Dunn, M. East, M. Effinger, R. Eng, G. Freebury, J. Garcia, J. Gaskin, S. Greene, J. Hennessy, E. Hilgemann, B. Hood, W. Holota, S. Howe, P. Huang, T. Hull, R. Hunt, K. Hurd, S. Johnson, A. Kissil, B. Knight, D. Kolenz, O. Kraus, J. Krist, M. Li, D. Lisman, M. Mandic, J. Mann, L. Marchen, C. Marrese-Reading, J. McCready, J. McGown, J. Missun, A. Miyaguchi, B. Moore, B. Nemati, S. Nikzad, J. Nissen, M. Novicki, T. Perrine, C. Pineda, O. Polanco, D. Putnam, A. Qureshi, M. Richards, A. J. Eldorado Riggs, M. Rodgers, M. Rud, N. Saini, D. Scalisi, D. Scharf, K. Schulz, G. Serabyn, N. Sigrist, G. Sikkia, A. Singleton, S. Shaklan, S. Smith, B. Southerd, M. Stahl, J. Steeves, B. Sturges, C. Sullivan, H. Tang, N. Taras, J. Tesch, M. Therrell, H. Tseng, M. Valente, D. Van Buren, J. Villalvazo, S. Warwick, D. Webb, T. Westerhoff, R. Wofford, G. Wu, J. Woo, M. Wood, J. Ziemer, G. Arney, J. Anderson, J. Maíz-Apellániz, J. Bartlett, R. Belikov, E. Bendek, B. Cenko, E. Douglas, S. Dulz, C. Evans, V. Faramaz, Y. K. Feng, H. Ferguson, K. Follette, S. Ford, M. García, M. Geha, D. Gelino, Y. Götberg, S. Hildebrandt, R. Hu, K. Jahnke, G. Kennedy, L. Kreidberg, A. Isella, E. Lopez, F. Marchis, L. Macri, M. Marley, W. Matzko, J. Mazoyer, S. McCandliss, T. Meshkat, C.

Mordasini, P. Morris, E. Nielsen, P. Newman, E. Petigura, M. Postman, A. Reines, A. Roberge, I. Roederer, G. Ruane, E. Schwieterman, D. Sirbu, C. Spalding, H. Teplitz, J. Tumlinson, N. Turner, J. Werk, A. Wofford, M. Wyatt, A. Young, and R. Zellem, "*The Habitable Exoplanet Observatory (HabEx) Mission Concept Study Final Report*," (Jet Propulsion Laboratory, 2019).

6. R. Juanola-Parramon, N. T. Zimmerman, L. Pueyo, M. Bolcar, G. Ruane, J. Krist, and T. Groff, "The LUVOIR Extreme Coronagraph for Living Planetary Systems (ECLIPS) II. Performance evaluation, aberration sensitivity analysis and exoplanet detection simulations," Proc. SPIE **11117**, 1111702 (2019).
7. L. Feinberg, B. Saif, B. Hayden, R. Keski-Kuha, M. Bluth, S. Park, and P. Greenfield, "Ultra-stable technology for high contrast observatories," Bull. Am. Astron. Soc. **51**, 12 (2019).